

Aging Effect of Catechol Redox Polymer Nanoparticles for Hybrid Supercapacitors

Antonela Gallastegui⁺^[a], Ousmane Camara⁺^[a, b], Daniela Minudri^[a], Nicolas Goujon^[a], Nagaraj Patil^[b], Fernando Ruipérez^[c], Rebeca Marcilla^[b] and David Mecerreyes^{*[a, d]}

Redox-polymer nanoparticles are a promising solution to avoid the detrimental dissolution of organic electrode materials while showing discrete redox processes. In this work, catechol-based redox-active polymer nanoparticles (cRPNs) were synthesized through one-step emulsion polymerization with a tunable size from 25 to 150 nm. The fresh cRPNs were characterized and showed a reversible redox process centered at 0.50 V (vs. Ag/AgCl) in 1 M H₂SO₄. Unexpectedly, the cRPN latex aged after days passing from white to pink. This aging resulted in a shift of

its redox potential toward higher values, which could be associated to autoxidation of the catechol groups and subsequent crosslinking of NPs due to catechol dimer formation. Finally, we compared the performance of fresh and aged cRPNs in a hybrid supercapacitor device, proving how the aging effect had some benefits such as an increase in the voltage output, specific capacitance, cyclability and Coulombic efficiencies of the device.

Introduction

In the last two decades, organic materials such as redox polymers have gained much interest as active compounds for electrochemical energy storage systems (EES). Inorganic materials currently used in these applications severely stress the raw material supply chain and present environmental issues related to their scarcity, toxicity (Co, V, Ni, etc.) and recycling limitation.^[1] Alternatively, organic compounds are composed of naturally abundant chemical elements (C, H, N, O, S) and if properly designed, they can even be generated from renewable resources.^[2] Their redox properties can be tailored in a straightforward way by adjusting the chemical composition and macromolecular architecture. Besides, organic molecules and redox polymers can show high theoretical capacity values

of up to 600 mAh g⁻¹, in comparison to inorganic cathodes (< 250 mAh g⁻¹)^[3] which makes them interesting for next-generation batteries and supercapacitors.^[3-6] However, they still show some performance limitations in terms of voltage, cyclability, self-discharge and reliability of the devices which curtails their commercial exploitation.

Among the different organic redox moieties, quinone functionalities can be readily accessible by the (electro)chemical oxidation of biopolymers such as lignins, tannins and phenolic compounds such as dopamine or catechols.^[7] Polymers containing quinone derivates have been gathering renowned interest as high-performance electrodes for EES because of their high theoretical specific capacity, structural diversity, tunable redox potentials and fast kinetics.^[8-11] In particular, within the family of quinones, *para*-quinone based redox-active polymers have received extensive research efforts for both capacitors and battery applications in recent years.^[12] *Ortho*-quinone based cathode materials are also attracting attention in pseudocapacitors and lithium-ion batteries.^[13,14] Indeed *ortho*-quinones show a stronger aromaticity of the reduce form that not only increases the redox potentials (thus, energy density), but also improves the reaction reversibility (thus, long cycle life) as compared to their *para*-counterparts.^[13-15] One popular bioinspired functional group that involves *ortho*-quinone structures is the catechol one, well known for its adhesive properties. Recently, polymers bearing catechol group have reported for aqueous rechargeable H⁺, Li-ion and post-Li-ion batteries^[16] thanks to their high theoretical capacity (up to 496 mAh g⁻¹) and their high redox potential at around 3.1 V (*ortho*-quinones vs. < 2.8 V for *para*-quinones) vs. Li/Li⁺.^[17,18]

A known issue of the use of organic materials as electrodes is the dissolution of the active material into the electrolyte which aggravates an adverse rapid capacity decay in the device. Several approaches have been adopted to minimize the

[a] Dr. A. Gallastegui,⁺ O. Camara,⁺ Dr. D. Minudri, Dr. N. Goujon, Prof. D. Mecerreyres

POLYMAT University of the Basque Country UPV/EHU
Av. Tolosa 72, 20018 San Sebastian, Spain

E-mail: David.mecerreyres@ehu.es

[b] O. Camara,⁺ Dr. N. Patil, Dr. R. Marcilla
Electrochemical Processes Unit, IMDEA Energy

Avenida Ramón de la Sagra 3, 28935 Móstoles, Madrid, Spain

[c] Dr. F. Ruipérez

POLYMAT and Physical Chemistry Department, Faculty of Pharmacy
University of the Basque Country UPV/EHU
01006 Vitoria-Gasteiz, Spain

[d] Prof. D. Mecerreyres

IKERBASQUE Basque Foundation for Science
48013 Bilbao, Spain

[+] These authors contributed equally to the work.

Supporting information for this article is available on the WWW under
<https://doi.org/10.1002/batt.202200155>

An invited contribution to a Special Collection on Organic Batteries.

© 2022 The Authors. *Batteries & Supercaps* published by Wiley-VCH GmbH.
This is an open access article under the terms of the Creative Commons Attribution License, which permits use, distribution and reproduction in any medium, provided the original work is properly cited.

dissolution issues, including, but not limited to the employment of redox polymers instead of small molecules,^[17] using redox active salts with low solubility or using solid polymer electrolytes instead of liquid one.^[20,21] Another interesting possibility to avoid further dissolution of the organic material is the use of cross-linked redox polymer nanoparticles (RPNs).^[22,23] Due to the versatility of polymer chemistry, RPNs can be designed with different different redox active groups (e.g., quinones, nitroxides)^[24,25] and sizes from nanometer to micrometer. This versatility makes RPNs excellent candidates for different electrochemical applications.

In this work, redox-active catechol-containing polymer nanoparticles (cRPNs) were synthesized through one step emulsion polymerization. This synthetic route allowed us to obtain latexes and polymer particles with a tuneable size (30–165 nm) without the need of cumbersome protection/deprotection chemistry of the catechol groups. After the cRPNs synthesis, we noticed that the latex solution turned from white to pink with time and this resulted in a shift on its redox potential toward more positive values. We investigated in detail this “aging effect” which may be associated to autoxidation and subsequent cross-linking of the catechol groups. Finally, performance of the fresh and aged cRPNs in hybrid supercapacitor device was compared, proving how the aging effect could help to improve the performance of the device.

Results and Discussion

Synthesis and characterization of catechol redox-active polymer nanoparticles (cRPNs) with different sizes

Catechol redox-active polymer nanoparticles (cRPNs) were synthesized through emulsion polymerization of dopamine methacrylamide (DMA) as shown in Scheme S1. This one-pot synthesis was carried out in water at 70 °C in 10% solids content, during 6 h, employing AIBA as initiator and CTAB as surfactant. It is important to remark that this method led to the one-pot-step synthesis of catechol polymer nanoparticles, without the need of additional catechol protection/deprotection steps. This is not a minor detail since it is known that catechols can interfere during radical polymerizations trapping the growing radical, limiting the conversion and producing cross-linked polymers. By increasing the concentration of CTAB cationic surfactant from 7.5×10^{-4} M to 2.5×10^{-3} M, the size of the particles could be controlled (see Table S1). Moreover, it is remarkable that besides this, we observed high reaction conversions in all the cases (> 75%). Thus, four different sizes of poly(dopamine methacrylamide) homopolymer particles were synthesized: cRPN-30, cRPN-60, cRPN-100 and cRPN-165, of which three of them were synthesized with surfactant and cRPN-165 without.^[23] The hydrodynamic diameter of the cRPNs within the aqueous latex was determined by DLS and their dried size by Transmission Electron Microscopy (TEM). As observed in Table S1, the cRPNs showed a particle size from 165 nm to a very small ones of 30 nm. As expected, the determined size through TEM was slightly lower than the one

obtained through DLS due to its drying process, leading to a smaller size of 157, 91, 52 and 25 nm, respectively. As shown in Figure 1d, the spherical shape of the nanoparticles is very clear, especially for the higher sizes of cRPNs. In the case of small cRPN-30, the latex TEM image is captured as a matrix of aggregated NP, probably due to its concentration, but nevertheless, a small well-defined spherical shape can be appreciated in the image. The polydispersity index (PDI) obtained by DLS was low for the bigger cRPNs but increased when smaller nanoparticles were obtained (see Table S1). This is an expected behaviour due to the employment of a higher quantity of surfactant needed for such small latexes.

Cyclic voltammetry (CV) in aqueous acidic media at room temperature was employed to investigate the effect of the particle size of the cRPNs in the electrochemical behaviour. For this measurement, cRPNs were formulated into conductive ink onto a glassy carbon electrode. Figure 1(a) shows as example the CVs recorded for cRPN-30 in 1 M H₂SO₄ at different scan rates (25–150 mV s⁻¹). The half-wave potential ($E_{1/2}$) was calculated using the expression (E_p forward + E_p backward)/2.

As observed, cRPN-30 presents a reversible redox process centered at $E_{1/2} = 0.54$ V (vs. Ag/AgCl), which is attributed to the removal/insertion of two electrons and two protons from/to catechol to/from *ortho*-quinone during the oxidation/reduction step (Figure 1b). The size of the catechol nanoparticles does not affect significantly the overall electrochemical behavior, all fresh cRPNs presented similar $E_{1/2}$, as observed in Figure S1, where the $E_{1/2}$ of reversible redox process is around 0.5 V.

The effect of scan rate on the electrochemical redox process of cRPNs of different sizes was investigated by cyclic voltammetry at different rates (Figure 1a). It can be observed that both current intensity and peak-to-peak potential separation increase gradually with the increase of the sweep rates. The plots of peak current intensity (I_p) against the square root of the potential scan rate ($v^{1/2}$) are shown in Figure 1(c) for all cRPNs, a linear relation was observed, which indicates that the electrochemical reaction at the electrode surface presents a diffusion-controlled process. On the other hand, from the slope of the linear correlation, it is possible to derive the magnitude of both cathodic and anodic diffusion coefficients through the Randles-Sevick equation:^[26,27]

$$I_p = 2.69 \times 10^5 n^{3/2} A \cdot C \cdot D^{1/2} v^{1/2},$$

where I_p is the peak current, A refers to the electrode surface area and C is the concentration of cRPNs. Therefore, with the constant parameters of A , C , and n , we could obtain an approximate value of D that is listed in Table S2.

Table S2 shows that the diffusion coefficient for the small cRPNs is higher than for the bigger nanoparticles. For cRPN-30 the cathodic value slope obtained is 3.09×10^{-4} , while for cRPN-165 is 1.05×10^{-4} , this clearly shows that the particle size affects directly on the diffusion process at room temperature. The increment of the anodic and cathodic diffusion coefficients for the smaller cRPNs is possibly due to a higher external surface area per volume of cRPNs in smaller NPs. This might afford shorter diffusion lengths for ion/electrons transport within the

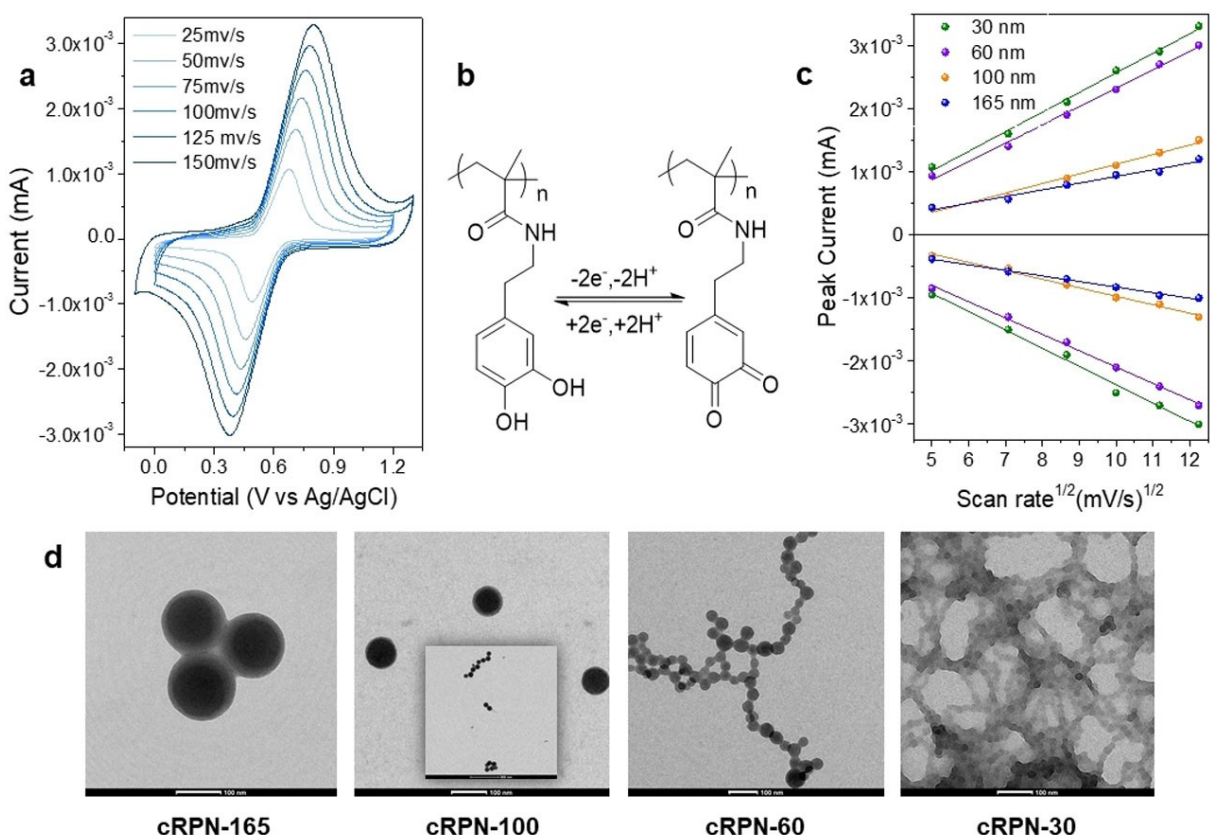


Figure 1. a) Cyclic voltammetry of cRPN-30 in 1 M H_2SO_4 at different scan rates (25–150 mV s^{-1}); b) reversible transformation of catechol to *ortho*-quinone; c) peak current (I_p) plot vs. scan rate (v); d) TEM images of cRPNs (scale bar: 100 nm).

inner bulk of NPs which is beneficial for the diffusion of charge carriers and electrons.

Aging of catechol latexes and cRPNs

As mentioned before, we observed that latexes evolved from a classic white color to pink over the days as shown in the picture of Figure 2. The smaller the size of the nanoparticles, the faster the latex became pinkish. While cRPN-165 needed 30 days for the color change, cRPN-30 needed only one week to show a pink latex color.

This unexpected aging effect was first investigated through UV-Vis as the spectra shown in Figure 2(a). Normally, catechol presents an absorbance peak around 270–290 nm. The spectrum of the latex at the time of its synthesis (0 day) presents an absorption peak at 288 nm, which increased in its intensity and become broader over time. As observed in the spectra, after 30 days, cRPN-165 presents a higher and wider absorbance peak around 288 nm. This change can be explained from the catechol chemistry. It is known that catechol undergoes cross-linking reactions in the presence of an oxidant like O_2 in basic medium.^[28,29] These cross-linking reactions are carried out, first, with the oxidation of the catechol to the quinone structure; as a second step, quinone undergoes a reverse dismutation reaction with another close catechol to form aryloxy radicals

that then dimerized to the dicatechol with the formation of a covalent bond (see Figure 3b).^[30] The formation of the dimer, normally promoted in basic medium, increases and broadens the absorbance peak.^[31,32] Thus, this aging effect observed over time is due to the auto-oxidation and subsequent cross-linking of the catechol moieties into catechol dimers in the presence of O_2 at neutral pH, increasing a 50% of its absorbance at 288 nm in the UV-Vis spectra.

After this observation, a proper comparison of fresh and aged cRPN was carried out. First, FT-Infrared Spectroscopy (FTIR) was carried out to corroborate the chemical composition of all the “fresh” catechol based cRPNs (0 day from their synthesis). As observed in Figure S2, the band at 785 cm^{-1} from DMA belongs to the bending vibration of the vinyl group ($\text{s}; \text{C}=\text{C}$ vinyl), which disappears after the synthesis, confirming the radical polymerization. A strong broad peak is observed in all cRPNs at 1638 cm^{-1} due to the amide carbonyl group stretching vibration ($\text{s}; (\text{HN}-\text{C}=\text{O})$), this peak can be observed at 1645 cm^{-1} in DMA monomer. Characteristics bands of DMA are present in all the nanoparticles: the peaks at 1522 and 1277 cm^{-1} are characteristics from the catechol ($\text{m}; (\text{C}=\text{C arom.})$).^[23] After the aging effect, FTIR was carried out to verify any change on the spectra. As observed in the Figure S3, at first sight, the spectrum between the aged and not aged nanoparticles do not show any significant difference, in fact, all the important peaks that belong to the correct catechol polymer

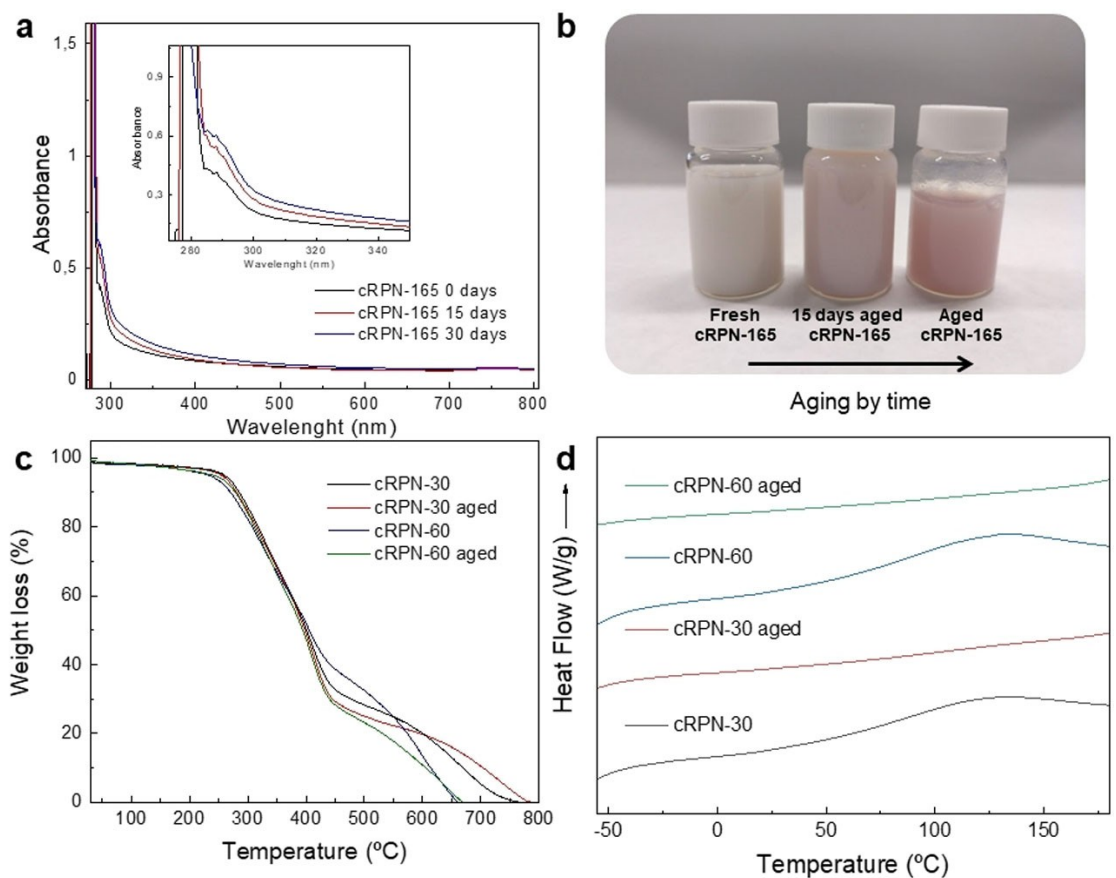


Figure 2. Uv-Vis spectra of a latex aqueous solution of cRPN-165 (a); the latexes correspond to different cRPN-165 synthesis over time, being the one on the left, the newest one (b); thermal characterization of cRPN-30 and cRPN-60 before and after aging effect: TGA (c) and DSC (d; second heating cycle) analysis.

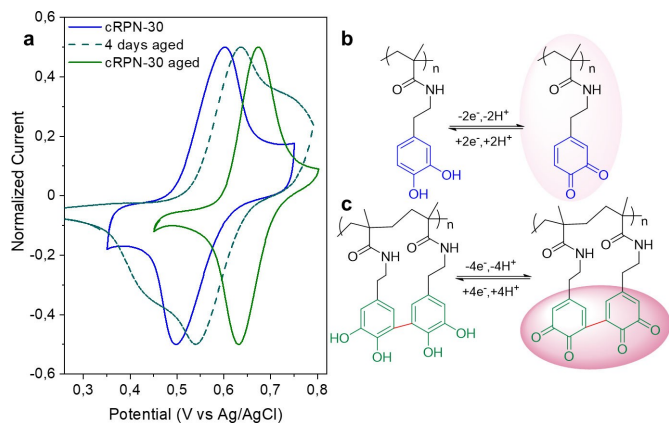


Figure 3. Cyclic voltammetry of “fresh” and “aged” cRPN-30 during different aging time (a); Scheme of oxidation/reduction process in the “fresh” nanoparticles (b); Scheme of dimer formation in “aged” nanoparticles (c).

nano particles are present in the aged nanoparticles spectra. When the region between 650 and 350 nm is expanded, below the fingerprint region, it is clear that an increase of peaks around 400 nm is shown (as example for cRPN-60 and cRPN-30). This peak increase at low wavenumber infrared region denotes the catechol dimer vibration formation (C–C between catechol groups) during the oxidation/cross-linking in water.

An increase of the peak at 1255 cm^{-1} is also observed due to the C–O–C stretching vibration as a product of cross-linking between catechol groups, as observed in Figure S3 (mild conditions) and Figure S4–S5 when cRPN-165 was abruptly exposed to oxygen and basic media (NaOH solution) in a short period of time.^[33] In these oxidant conditions, the increase of this peak is clearly observed.

The thermal behavior of the polymer nanoparticles was also analyzed. Figure S6 shows the thermal degradation through TGA technique of all “fresh” cRPNs before aging effect. It can be appreciated that the degradation onset of all nanoparticles starts at around 250°C and a 50% degradation weight loss is obtained at about 400°C . All cRPNs presents a good thermal stability also after the aging effect as observed in Figure 2c. After the aging process, the degradation temperature did not change at all, reaching a total decomposition at the same temperature. When DSC was carried out, there was a clear change on the response of the heat flow versus temperature curve when cRPNs suffered aging. As appreciated in Figure 2d, cRPN-30 and cRPN-60 present a T_g at around 120°C that disappears later when cRPNs are aged. This result agrees with the fact that the catechol dimer formation formed over time generates a more cross-linked NP that does not allow the polymer chains to relax as in the “fresh” NPs. This crosslinking leads to the disappearance of the T_g . Same behavior was also

observed for cRPN-100 and cRPN-165, shown in Figure S7, where the Tg change was not so evident for the biggest size of cRPNs.

Finally, Figure S8 shows a TEM picture of cRPN-165 after 30 days of aging, a picture in which is clearly shown that the nanoparticles seem to be attached or polymerically bonded, as expected, since catechol can undergo dimer formation during the oxidation/cross-linking process, which may happen inside the nanoparticles and between them, as observed in the picture.

Cyclic voltammetry was carried out to study the effect of the aging of cRPNs on their redox behaviour. Figure 3a shows the CVs recorded for fresh and aged cRPN-30 in 1 M H₂SO₄ at a scan rate of 50 mV/s. Differences in the redox potentials are directly related to the aging time of the nanoparticles.

Fresh nanoparticles are able to oxidize/reduce with $E_{1/2}$ around 0.54 V (blue line) as mentioned before, corresponding to the catechol/ortho-quinone transformations (Figure 3b), whereas after 4 days of aging the $E_{1/2}$ is displaced to a positive shift and another peak appears as a consequence of the internal cross-linking (light blue line). Finally, after one week, when the nanoparticles are aged at its maximum, the redox potential is established at $E_{1/2}=0.65$ V (green line). Similar voltammograms were observed for cRPN-60 (see Figure S9), which needed two weeks for its maximum extent of aging.

In order to understand this redox potential shift, DFT calculations were carried out, using a simplified model of the redox polymer, including none (see Figure 3b) or two linked catechols (see Figure 3c), that will be referred as monomer and dimer, respectively, hereafter. The calculated redox potential (vs SHE) for the bare catechol is 0.02 V, while that for the dimer is increased to 0.35 V. This enhancement can be explained by the presence of hydrogen bonds between adjacent catechols. Thus, it is reasonable to assume that some of the electroactive groups will be in the reduced form (catechol), while others will be in the oxidized form (quinone). The hydrogen bond between a catechol -OH moiety and the adjacent carbonyl moiety (O=C) may assist the redox process, whether it's the reduction of the quinone or the oxidation of the catechol. Thus, when a quinone carbonyl is reduced, the -OH moiety of an adjacent catechol can stabilize the generated anion by hydrogen bonding, facilitating the process and, therefore, larger redox potentials are observed. In an isolated catechol, this extra stabilization is absent, and the redox potential is lower.

In Figure S10 is represented the molecular model and the atoms involved in the process are highlighted in red. In Table S3 the geometrical parameters of the dimer during the reduction process of a quinone moiety are collected, where R(C=O) and R(O-H) correspond to the bond distances in the C-OH moiety of the catechol, R(OH...O=C) is the bond distance of the hydrogen bond between the OH and the carbonyl (C=O), and R(O=C) is the carbonyl bond distance. Thus, we can observe how these parameters are modified during the two-electron reduction process from the quinone (Q) to the semiquinone (SQ) and the catechol (QH₂). Before the redox process takes place, we found a hydrogen bond distance of 1.646 Å that is remarkably decreased when the quinone is

reduced to a semiquinone (1.354 Å). This hydrogen bond stabilizes the SQ and facilitates the reduction. At the same time, the carbonyl double bond is enlarged from 1.225 to 1.277 Å, while the C–O bond in the catechol is shortened (from 1.358 to 1.342 Å). In the second step, the SQ is reduced to catechol (QH₂) and the hydrogen is completely transferred (1.002 Å) yielding a new OH moiety.

Catechol based RPNs for hybrid Supercapacitors

As shown before, the unexpected aging effect increases the redox potential of catechol based redox polymer nanoparticles in acid electrolyte. Interestingly, this can be beneficial for its application as positive electrode (cathode) in electrochemical energy storage systems (EES). To demonstrate its applicability at the device level, we assembled an unoptimized hybrid supercapacitor as a representative example of EES (Figure 4a). This hybrid supercapacitor is based on an Activated Carbon (AC) electrode as negative electrode and the buckypaper with fresh/aged cRPN-30 as positive electrode using 1 M H₂SO₄ aqueous electrolyte. Figure 4b shows the CV of supercapacitors assembled with "fresh" and "aged" nanoparticles. CVs of both fresh and aged cRPN-30 show reversible redox behavior with a pair of redox peaks centered at $E_{1/2}=-27$ mV (vs AC) and $E_{1/2}=+74$ mV, respectively. This result in a relative voltage gain of ~100 mV for the supercapacitor using "aged" NPs. That is in good agreement with the observations made in the preliminary electrochemical characterization (three electrode configuration), confirming that the aging effect has the advantage of enhancing the voltage output of the supercapacitor.

The capacity retention of the fresh and aged cells over 180 galvanostatic charge-discharge cycles was compared in Figure 4d (the individual cycling performances including coulombic efficiencies can be found in Figure S11). In the case of fresh cRPN-30, there is a significant decay of the capacity within the first few cycles probably due to some nanoparticles dissolution. Interestingly, this does not happen with aged nanoparticles and their capacity retention is excellent probably due to their more cross-linked nature. Furthermore, Coulombic efficiencies (CE) for the cross-linked cRPN-30 were found to be higher (> 96%), while the average CE for the corresponding fresh nanoparticles remained below 85% (Figure S11).

In Figure 4c, we plot the comparison between the performance of fresh and aged cells at different current densities. It is worth to note than the theoretical capacity of the catechol NP is 245 mAh/g. This graph is plotted from the Rate Capability plots from Figure S12. Every point of the graph corresponds to a fixed specific capacitance (or capacity) value at the 5th cycle of a well-defined current density, and the following general observations can be made: i) capacity at a low current density of 0.2 A/g was over 2-fold higher for the aged cRPN-30 (140 mAh g⁻¹/625 F g⁻¹) compared to the fresh one (57 mAh g⁻¹/225 F g⁻¹), ii) the capacities at all the higher current densities were also higher for the aged over fresh nanoparticles, and iii) the CEs at all the current densities were also higher for the aged over fresh nanoparticles.

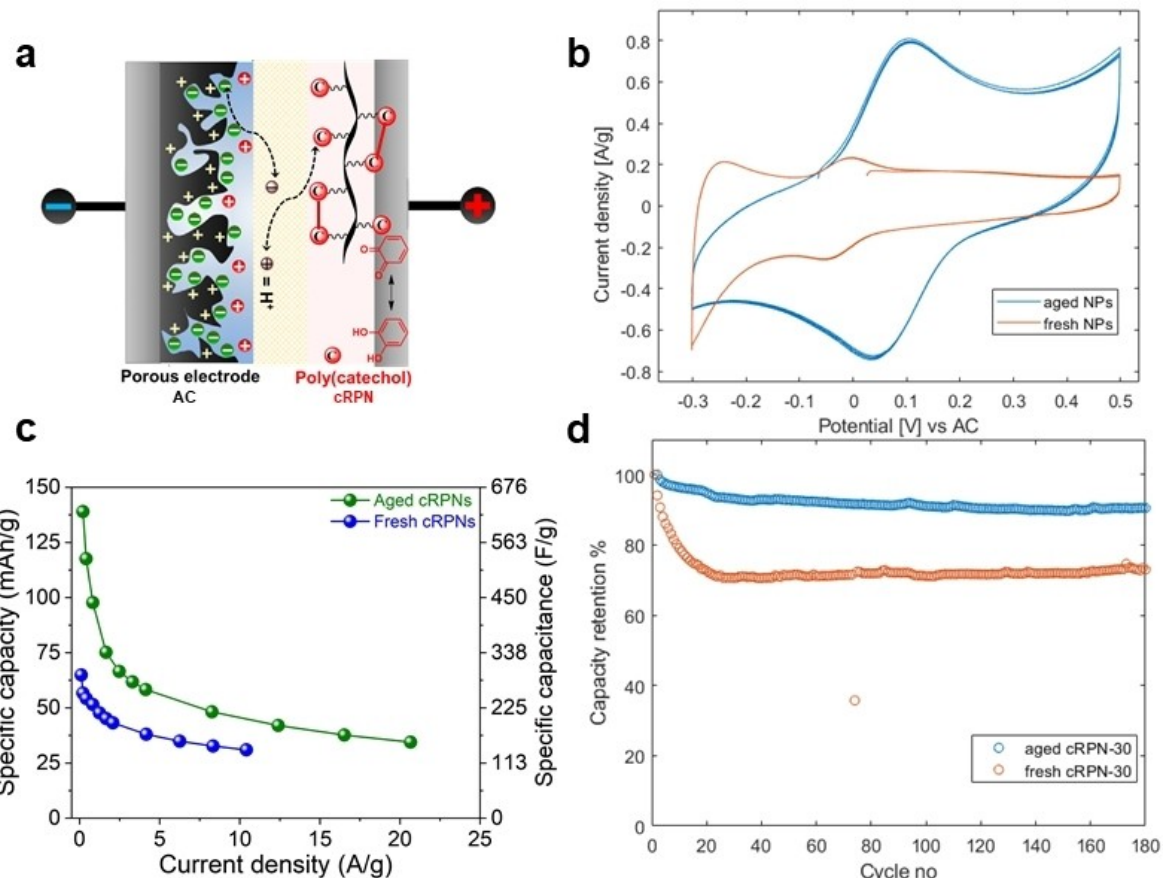


Figure 4. Scheme of the hybrid supercapacitor (a); Cyclic voltammetry of the hybrid supercapacitors (b); Comparison of specific capacitance/capacity at different current density values of the AC//polymer device in aged and fresh conditions (c); and their cycling stability, depicting discharge capacity retention (d) in fresh and aged conditions.

This improved rate performance for Aged cRPNs over Fresh cRPNs was corroborated also by electrochemical impedance spectroscopy (EIS). All the Nyquist plots feature two well-defined regions: a depressed semicircle in the high frequency region and an inclined line in the low-frequency that provide information about the charge-transfer resistance (R_{ct}) and Warburg impedance (Figure S13, Supplementary Information).^[34–35] Aged cRPN exhibited lower R_{ct} compared to fresh cRPNs ($2.54\ \Omega$ and $5.15\ \Omega$, respectively), this result is in line with the obtained results from the cycling, in fact a lower R_{ct} means a better kinetics and a better rate capability, all visible effects when comparing with the rate capability tests and the cyclings.

Conclusion

In conclusion, this article reports the synthesis of catechol redox polymer poly(dopamine methacrylamide) nanoparticles in one pot-step with sizes between 30 to 150 nm. Unexpectedly, we observed an aging effect of the catechol-based redox-active nanoparticles which latexes turned from white to pink. This color change was associated with the dimerization of the catechol groups in the NPs. All cRPNs were properly charac-

terized, showing that the dimer formation process can be analysed through FTIR, UV-Vis spectrophotometry and thermal analysis. The electrochemical characterizations of the redox-active polymer nanoparticles show that the redox potentials increased from 0.50 V (vs Ag/AgCl) to 0.65 V due to the aging. This shifting of redox potential was predicted theoretically by DFT calculations. Finally, the benefit of the aging effect on the electrochemical performance of cRPNs as cathodes in supercapacitor device was demonstrated. The aged redox polymer nanoparticles not only showed higher redox potential, but also higher capacities and better retention upon cycling compared to the fresh ones (higher coulombic efficiencies). These results highlight the simple, yet effective way of enhancing electrochemical performance of catechol-based polymers through the demonstrated aging effect. We also hypothesized that this concept can be extended to other types of EES, for instance, to innovative proton batteries, using our cRPN as a proton host high voltage cathode, broadening their scope as advanced organic electrodes.^[36]

Experimental Section

Materials and methods

Materials

Dopamine-HCl and MgSO₄ were obtained from Alfa Aesar. Methanol, ethyl acetate, acetonitrile (MeCN) and absolute ethanol were purchased from Acros. 2,2'-azobis(2-methylpropionamidine) dihydrochloride (AIBA), hexadecyltrimethylammonium bromide (CTAB), N-methyl-2-pyrrolidone (NMP) and polyvinylidene fluoride (PVDF) were purchased on Sigma Aldrich. Large surface area single wall carbon nanotubes (SWCNTs) and reduced graphene oxide (RGO) were purchased from Nanografi. All the chemicals and solvents were employed as received without further purification.

Dopamine methacrylamide (DMA) was synthesized by a protocol described by Nguyen et al.^[37] The monomer was successfully characterized by proton NMR analysis. ¹H-NMR (DMSO-d₆, 400 MHz): δ 8.7–8.6 (2H), 7.9 (1H), 6.4–6.6 (2H), 6.42 (1H), 5.62 (1H), 5.31 (1H), 3.24 (2H), 2.51 (2H), 1.85 (3H), as shown in our previous work.^[23]

Synthesis of cRPNs

cRPNs were synthesized by emulsion polymerization in aqueous media at 70 °C, employing unprotected DMA and CTAB as surfactant at different concentration targets (from 7.5 × 10⁻⁴ M to 0.0025 M) depending on the desired size of the nanoparticles. During the synthesis, Scheme S1, 0.03 mmol (1 × 10⁻³ M) of AIBA pre-dissolved in 25 mL of Milli-Q water was vigorous stirred with a deoxygenation process employing N₂ during 30 min. At 55 °C, a solution of unprotected DMA dissolved in methanol (0.1 g mL⁻¹) was injected at 2 mL min⁻¹ into the reaction mixture employing an automatic syringe pump. At the end of the injection, the reaction mixture reached 70 °C, which was left during 6 h. A total monomer concentration of 1 mmol (4 × 10⁻² M) was employed. The nanoparticles were then purified with Milli-Q water during 6 days at 25 °C employing dialysis tubes with a molecular weight cut-off of 14000 Da and finally freeze-dried with a Telstar LyoQuest-85 Lyophilizer at –80 °C and 0.082 mbar during 3 days.

Characterization procedures

The hydrodynamic size of the different catechol RPNs were measured by dynamic light scattering (DLS) using a Malvern Zetasizer Nano ZS. A drop of reaction mixture (0.1 mL of the dispersion in water) was diluted with 3 mL of Milli-Q water employing disposable polystyrene cuvettes DTS0012. The intensity average was measured at 25 °C and 173° backscatter angle by using dynamic light scattering Malvern ZetaSizer Nano-S instrument equipped with a 633 nm red laser.

The diameter and the morphology of the dried nanoparticles were measured also by transmission electron microscopy (TEM) employing a TECNAI G2 20 TWIN (200 kV). The samples were deposited on copper grids and left dry at room temperature before the measurements.

Fourier transform infrared (FTIR) spectra were measured on a Bruker Alpha II spectrophotometer employing Platinum ATR module with diamond window. Between 2 and 5 mg of each sample were employed for the characterization.

UV-Vis spectroscopy measurements of the cRPNs solutions were performed on a Hewlett Packard (HP) model 8453 spectrophotometer.

The thermal stability of the cRPNs was investigated by thermogravimetric analysis (TGA) performed on a TGA Q500 from TA Instruments. The samples were heated at 10 °C min⁻¹ under N₂ atmosphere from room temperature to 800 °C.

Differential scanning calorimetry (DSC) was employed to detect the T_g of the samples by measurements on a DSC Q2000 from TA Instruments. The DSC scans were performed at heating and cooling rates of 10 °C min⁻¹ from –60 °C to 200 °C. Between 5 and 10 mg of each cRPNs were employed for the measurement. T_g was determined for the second heating cycle employing the middle temperature.

Quantum chemical calculations

Geometry optimizations have been performed in gas phase within density functional theory (DFT) using the B3PW91 functional in combination with the 6-31+G(d) basis set.^[38–41] Harmonic vibrational frequencies were obtained at the same level of theory to confirm that all the structures were minima in the potential energy surfaces (no imaginary frequencies were found), to evaluate the zero-point vibrational energy (ZPVE) and the thermal corrections to the Gibbs free energy (298 K, 1 atm) in the harmonic oscillator approximation. Single-point calculations using the aug-cc-pVTZ basis set were carried out on the optimized structures to refine the electronic energy.^[42] Solvent effects in acetonitrile have been estimated using the polarizable continuum model (PCM) approach.^[43–46]

All calculations were performed using the Gaussian 16 suit of programs.^[47]

Electrochemical characterization

Cyclic voltammetry (CV) was performed using Autolab PGSTAT204 potentiostat/galvanostat, in a conventional three electrode cell. A glassy carbon disk (GC; surface area of 0.28 cm²) was modified with slurry containing cRPNs and used as working electrode. Before modification, the GC electrode was polished using 0.3 μm alumina and sequentially sonicated in water and absolute ethanol. A platinum wire, and Ag/AgCl (3 M KCl) electrode were the counter and reference electrodes, respectively.

The slurry was prepared employing 10 mg of redox-active catechol nanoparticles (50 wt.%), 8 mg of conductive carbon black C65 (40 wt.%) and 2 mg of PVDF (10 wt.%). They were dispersed in 500 μL of NMP by magnetic stirring for 30 min to form a uniform suspension. Then, the slurry was dropped on the top of the GC electrode and dried under vacuum at 50 °C for 30 min. The electrode was used immediately after drying as the working electrode.

Electrochemical characterization of hybrid supercapacitor

The hybrid supercapacitor was assembled into CR 2032 coin-type cells using the activated carbon electrode previously prepared in the negative side of the cell, a porous Whatman glass microfiber filters (Grade GF/B) soaked with 200 μL of electrolyte (1 M H₂SO₄ in water) and the buckypaper previously prepared in the positive electrode side. The CV of the hybrid supercapacitor was performed with a Bio-logic VMP3 multichannel Potentiostat/Galvanostat (Bio-logic SP150). The cycling and rate performance of coin-type hybrid supercapacitor were assessed by galvanostatic charge-discharge (GCD) experiments with a Neware battery cycler at 25 °C. As a commonly used procedure for polymer-based organic electrodes, the specific capacity (mAh g⁻¹)/capacitance (F g⁻¹) and specific

current (Ag^{-1}) were normalized with respect to the polymer mass in the cathode.

The EIS data were collected in the $0.1\text{--}2\times10^5$ Hz frequency range using a sinusoidal signal with an amplitude of XX mV at equilibrium discharge potential (-0.5 V against active carbon; $\sim 50\%$ depth-of-discharge). First, the EIS measurement of activated carbon || cRPN cells were carried out for both fresh and aged cRPN-30 at 0.5 V vs AC, voltage in which the nanoparticles are partially in a charged state.

Preparation of cRPNs for supercapacitors

The activated carbon electrode was prepared employing 3 g of activated carbon (80 wt.%) (NORIT DLC SUPRA 50 94008-5), 300 mg of carbon black (8 wt.%) and 450 mg of PVDF (12 wt.%). The first two components were ball milled together in a Retsch Planetary Ball Mill PM100 (400 rpm, 30 min), then the binder was added with NMP until obtaining a uniform slurry. The slurry was casted on carbon cloth (Etek Cloth B; Fuel Cell Earth) through doctor blade technique with a thickness of $250\ \mu\text{m}$, dried at 60°C for 6 h, then left at 80°C overnight under vacuum and finally left at 120°C for 6 h under vacuum. After drying, the cloth is punched into circular electrodes with 10 mm diameter which are employed as counter electrodes in a coin cell.

In order to make the buckypaper electrode, first, 15 mg of SWCNTs are dispersed in 20 mL solution of IPA/NMP (1/1 v/v) through a tip sonicator for 10 min, half power, half amplitude (ultrasonic processor UP400S, 400 W, 24 kHz), then, after carefully grinding 5 mg of rGO with 2.5 mg of cRPNs, those are added to the sonicated solution and then sonicated again. After, this solution is immersed in a bath sonicator (Branson 2510, 100 W, 42 kHz) for 2 h, then stirred overnight to prepare the electrode ink. The next step is the filtration of the electrode ink. The suspension was filtered through a Nylon membrane filter (47 mm diameter, pore size $0.45\ \mu\text{m}$) with the help of vacuum, followed by thorough rinsing with isopropanol to remove loosely bound polymer. The buckypaper was carefully peeled-off from the filter and dried overnight at 60°C under vacuum. The buckypaper was cut into circular discs with a diameter of 8 mm. A control buckypaper was used without adding cRPNs, employing the same procedure as mentioned. Electrode mass loading is $2.7\ \text{mg}/\text{cm}^2$.

Acknowledgements

The authors thank for technical and human support provided by IZO-SGI SGIker of UPV/EHU. Technical and human support provided by IZO-SGI, SGIker (UPV/EHU, MICINN, GV/EJ, ERDF and ESF) is gratefully acknowledged for assistance and generous allocation of computational resources. The authors would like to thank the European Commission for financial support through funding from the European Union's Horizon 2020 research and innovation program under the Marie Skłodowska-Curie grant agreement No 823989. N.P. appreciates Spanish MINECO for the Juan de la Cierva-formation fellowship (FJC2018-037781-I). R.M. thanks the Spanish Ministry of Science, Innovation and Universities through the SUSBAT project (Ref.RTI2018-101049-B-I00) (MINECO/FEDER, UE) for financial support.

Conflict of Interest

The authors declare no conflict of interest.

Data Availability Statement

The data that support the findings of this study are available on request from the corresponding author. The data are not publicly available due to privacy or ethical restrictions.

Keywords: redox-active polymer nanoparticles • catechol crosslinking • supercapacitor

- [1] P. Poizot, J. Gaubicher, S. Renault, L. Dubois, Y. Liang, Y. Yao, *Chem. Rev.* **2020**, *120*, 6490–6557.
- [2] B. Häupler, A. Wild, A. Schubert, *Adv. Energy Mater.* **2015**, *5*, 1402034.
- [3] F. N. Ajjan, D. Mecerreyes, O. Inganäs, *Biotechnol. J.* **2019**, *14*, 1900062.
- [4] A. M. Navarro-Suárez, J. Carretero-González, N. Casado, D. Mecerreyes, T. Rojo, E. Castillo-Martínez, *Sustain. Energy Fuels* **2018**, *2*, 836.
- [5] C. Fribe, A. Lex-Balducci, U. S. Schubert, *ChemSusChem* **2019**, *12*, 4093.
- [6] Y. Y. Lai, X. Li, Y. Zhu, *ACS Appl. Polym. Mater.* **2020**, *2*, 113.
- [7] N. Goujon, N. Casado, N. Patil, R. Marcilla, D. Mecerreyes, *Prog. Polym. Sci.* **2021**, *122*, 101449.
- [8] E. J. Son, J. H. Kim, K. Kim, C. B. Park, *J. Mater. Chem. A* **2016**, *4*, 11179.
- [9] Y. Wu, R. Zeng, J. Nan, D. Shu, Y. Qiu, S. L. Chou, *Adv. Energy Mater.* **2017**, *7*, 1700278.
- [10] T. Sun, J. Xie, W. Guo, D. Li, Q. Zhang, *Adv. Energy Mater.* **2020**, *10*, 1904199.
- [11] J. Xie, Z. Wang, Z. J. Xu, Q. Zhang, *Adv. Energy Mater.* **2018**, *8*, 1703509.
- [12] N. Patil, R. Marcilla, *Redox Polymers for Energy and Nanomedicine*, **2020**, chapter 7.
- [13] D. M. Anjos, J. K. McDonough, E. Perre, G. M. Brown, S. H. Overbury, Y. Gogotsi, V. Presser, *Nano Energy* **2013**, *2*, 702.
- [14] T. Nokami, T. Matsuo, Y. Inatomi, N. Hojo, T. Tsukagoshi, H. Yoshizawa, A. Shimizu, H. Kuramoto, K. Komae, H. Tsuyama, J. Yoshida, *J. Am. Chem. Soc.* **2012**, *134*, 19694.
- [15] Y. Liang, Y. Jing, S. Gheytani, K. Y. Lee, P. Liu, A. Facchetti, Y. Yao, *Nat. Mater.* **2017**, *16*, 841.
- [16] N. Patil, A. Mavrandonakis, C. Jérôme, C. Detrembleur, J. Palma, R. Marcilla, *ACS Appl. Energ. Mater.* **2019**, *2*, 3035.
- [17] L. Zhu, G. Ding, L. Xie, X. Cao, J. Liu, X. Lei, J. Ma, *Chem. Mater.* **2019**, *31*, 8582.
- [18] H. Wang, R. Emanuelsson, H. Liu, K. Edström, F. Mamedov, M. Strømme, M. Sjödin, *ACS Appl. Energ. Mater.* **2019**, *2*, 7162.
- [19] Y. Liang, Y. Yao, *Joule* **2018**, *2*, 1690.
- [20] Z. Zhu, M. Hong, D. Guo, J. Shi, Z. Tao, J. Chen, *J. Am. Chem. Soc.* **2014**, *136*, 16461.
- [21] X. Chi, Y. Liang, F. Hao, Y. Zhang, J. Whiteley, H. Dong, P. Hu, S. Lee, Y. Yao, *Angew. Chem. Int. Ed.* **2018**, *57*, 2630.
- [22] K. Pirnat, N. Casado, L. Porcarelli, N. Ballard, D. Mecerreyes, *Macromolecules* **2019**, *52*, 8155.
- [23] A. Gallastegui, D. Minudri, N. Casado, N. Goujon, F. Ruipérez, N. Patil, D. Mecerreyes, *Sustain. Energy Fuels* **2020**, *4*, 3934.
- [24] S. Muench, P. Gerlach, R. Burges, M. Strumpf, S. Hoeppener, A. Wild, A. Lex-Balducci, A. Balducci, J. C. Brendel, U. S. Schubert, *ChemSusChem* **2021**, *14*, 449.
- [25] B. Häupler, A. Wild, U. S. Schubert, *Adv. Energy Mater.* **2015**, *5*, 1402034.
- [26] A. J. Bard, L. R. Faulkner, *Electrochemical methods: fundamentals and applications*, 2nd ed., Wiley, New York, 1980.
- [27] H. Wang, S. Y. Sayed, E. J. Luber, B. C. Olsen, S. M. Shirurkar, S. Venkatakrishnan, U. M. Tefashe, A. K. Farquhar, E. S. Smotkin, R. L. McCreery, J. M. Buriak, *ACS Nano* **2020**, *14*, 2575.
- [28] S. Haemers, G. J. M. Koper, G. Frens, *Biomacromolecules* **2003**, *4*, 632.
- [29] B. P. Lee, J. L. Dalsin, P. B. Messersmith, *Biomacromolecules* **2002**, *3*, 1038.
- [30] M. Masaki, H. Uyama, A. J. van der Vlies, U. Hasegawa, *Colloid Polym. Sci.* **2015**, *293*, 1245.
- [31] M. C. Van der Leeden, *Langmuir* **2005**, *21*, 11373.

- [32] B. P. Lee, J. L. Dalsin, P. B. Messersmith, *Biomacromolecules* **2002**, *3*, 1038.2.
- [33] H. Luo, C. Gu, W. Zheng, F. Dai, X. Wang, Z. Zheng, *RSC Adv.* **2015**, *5*, 13470.
- [34] M. Zhu, L. Zhao, Q. Ran, Y. Zhang, R. Peng, G. Lu, X. Jia, D. Chao, C. Wang, *Adv. Sci.* **2022**, *9*, 2103896.
- [35] N. Patil, A. Agil, F. Ouhib, S. Admassie, O. Inganäs, C. Jérôme, C. Detrembleur, *Adv. Mater.* **2017**, *29*, 1703737.
- [36] R. Grieco, A. Molina, J. S. Sanchez, N. Patil, M. Liras, R. Marcilla, *Mater. Today* **2022**, *27*, 101014.
- [37] H. N. Nguyen, E. T. Nadres, B. G. Alamani, D. F. Rodrigues, *J. Mater. Chem. B* **2017**, *5*, 6616.
- [38] A. D. Becke, *Phys. Rev. A* **1988**, *38*, 3098–3100.
- [39] J. P. Perdew, in *Electronic structure of solids* (Eds. P. Ziesche and H. Eschig), Akademie Verlag, Berlin, **1991**.
- [40] K. Burke, J. P. Perdew, Y. Wang, in *Electronic density functional theory: recent progress and new directions*, (Eds. J. F. Dobson, G. Vignale, M. P. Das), Plenum, New York, **1998**.
- [41] W. J. Hehre, R. Ditchfield, J. A. Pople, *J. Chem. Phys.* **1972**, *56*, 2257–2261.
- [42] D. E. Woon, T. H. Dunning Jr., *J. Chem. Phys.* **1993**, *98*, 1358–1371.
- [43] M. Cossi, V. Barone, R. Cammi, J. Tomasi, *Chem. Phys. Lett.* **1996**, *255*, 327.
- [44] E. Cancès, B. Mannucci, J. Tomasi, *J. Chem. Phys.* **1997**, *107*, 3032.
- [45] V. Barone, M. Cossi, J. Tomasi, *J. Chem. Phys.* **1997**, *107*, 3210.
- [46] V. Barone, M. Cossi, J. Tomasi, *J. Comput. Chem.* **1998**, *19*, 404.
- [47] Gaussian 16, Revision C.01, M. J. Frisch, G. W. Trucks, H. B. Schlegel, G. E. Scuseria, M. A. Robb, J. R. Cheeseman, G. Scalmani, V. Barone, G. A. Petersson, H. Nakatsuji, X. Li, M. Caricato, A. V. Marenich, J. Bloino, B. G. Janesko, R. Gomperts, B. Mennucci, H. P. Hratchian, J. V. Ortiz, A. F. Izmaylov, J. L. Sonnenberg, D. Williams-Young, F. Ding, F. Lipparini, F. Egidi, J. Goings, B. Peng, A. Petrone, T. Henderson, D. Ranasinghe, V. G. Zakrzewski, J. Gao, N. Rega, G. Zheng, W. Liang, M. Hada, M. Ehara, K. Toyota, R. Fukuda, J. Hasegawa, M. Ishida, T. Nakajima, Y. Honda, O. Kitao, H. Nakai, T. Vreven, K. Throssell, J. A. Montgomery, Jr., J. E. Peralta, F. Ogliaro, M. J. Bearpark, J. J. Heyd, E. N. Brothers, K. N. Kudin, V. N. Staroverov, T. A. Keith, R. Kobayashi, J. Normand, K. Ragahavachari, A. P. Rendell, J. C. Burant, S. S. Iyengar, J. Tomasi, M. Cossi, J. M. Millam, M. Klene, C. Adamo, R. Cammi, J. W. Ochterski, R. L. Martin, K. Morokuma, O. Farkas, J. B. Foresman, D. J. Fox, Gaussian, Inc., Wallingford CT, **2016**.

Manuscript received: April 1, 2022
 Revised manuscript received: May 13, 2022
 Accepted manuscript online: May 20, 2022
 Version of record online: June 15, 2022